Realistic quantum design of silicon quantum dot intermediate band solar cells

Realistic quantum design of silicon quantum dot intermediate band solar cells

Weiguo Hu[1,2], Makoto Igarashi[1,2], Ming-Yi Lee[3], Yiming Li[3,4] and Seiji Samukawa[1,2,4]

[1] Institute of Fluid Science, Tohoku University, 2-1-1 Katahira, Sendai, Miyagi 980-8577, Japan
[2] Japan Science and Technology Agency (JST), CREST, 5 Sanbancho, Chiyoda, Tokyo 102-0075, Japan
[3] Department of Electrical and Computer Engineering, National Chiao Tung University, Hsinchu 300, Taiwan
[4] WPI Advanced Institute for Materials Research, Tohoku University, 2-1-1 Katahira, Sendai, Miyagi 980-8577, Japan

E-mail: ymli@faculty.nctu.edu.tw and samukawa@ifs.tohoku.ac.jp

Abstract

A highly periodical Si nanodisk superlattice has been fabricated by our top-down process. Based on the realistic structure, a 3D simulation program using the finite element method is developed to calculate energy band structure, optical and electrical properties, as well as the intermediate band solar cell operation. Both the experiments and simulations reveal that miniband formation enhances the optical and electrical collections. Consequently, detailed electronic structure and conversion efficiency are examined to guide the optimal design of minibands. A theoretically predicted maximal efficiency of the explored Si nanodisk superlattice is 50.3%, which is promising, compared with well-known complicated Si tandem solar cells.

1. Introduction

Very recently, Si-based solar cell efficiency reached up to 25.0%, which is approaching the Shockley–Queisser (S–Q) limit [1]. The quantum dot (QD) solar cell has become a promising candidate to break this limit for a competitive commercial cost of unit power [2–10]. The well aligned QD superlattice is expected to form minibands between the valence band (VB) and the conduction band (CB), which induces an extra two-photon-transition from VB to CB via IB, the so-called intermediate band solar cell (IBSC) [2–4]. Intrinsically, this novel cell combines two low-energy photons to generate a pair of high-energy electron–hole pairs to produce additional photocurrent without degrading the photovoltaic cell. Several prototype cells have been fabricated with mature In(Ga)As QDs to prove the core two-photon-transition process [5–7]. However, their conversion efficiency does not greatly exceed that of well-developed traditional cells. A key issue of new research is to design and optimize device structure to gradually approach its theoretical efficiency. The devices face a great challenge from QD superlattices in terms of fabrication and simulation.

Even well-developed molecular beam epitaxy (MBE) has also failed to fabricate an ideal QD superlattice. Limited to the growth kinetic of Stranski–Krastanov (SK) growth, MBE cannot control the growth direction alignment any more than random in-plane distributions, which hardly satisfies the precondition of miniband formation [11]; in addition, the necessary wetting layer induces a 1D quantum state to complicate zero-state sub-bandgap design in IBSCs [12]. Simultaneously, theoretical models have been developed but they are still insufficient; most studies well describe macroscopic device operations such as two-photon-transition and carrier drift/diffusion, but neglect quantum process such as quantum confinement, tunneling and miniband structure [13–17]; some studies mainly focus on optical absorption and carriers' localization/extraction in ideal superlattices [18–20]. Recently, the classic Kronig–Penney model has tentatively been integrated in the device model to calculate a simple 1D superlattice [21].

Obviously, a Si-based IBSC has the greater potential in commercial applications due to the abundance of Si and the mature device process. However, complex band structure (in-direct bandgap) and difficult nanotechnology
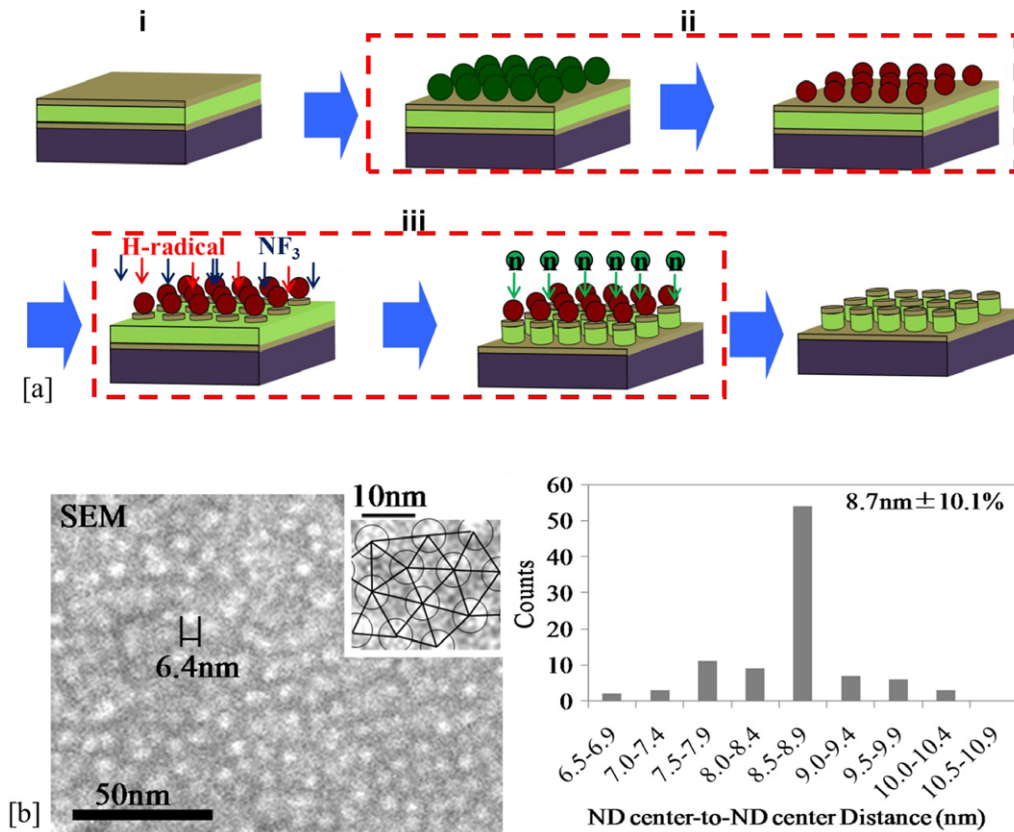
Figure 1. An advanced top-down nano-fabrication technology. (a) Fabrication flow of the Si-NDs superlattice, which includes (i) Si film deposition and surface oxidation, (ii) a 2D array ferritin self-assembly and protein shell removal, (iii) NF$_3$ treatment to remove the surface SiO$_2$ and NB etching to remove the poly-Si. Finally, we can re-deposit various matrices such as SiO$_2$, SiN and SiC to cover the Si-NDs superlattice. (b) SEM image and statistics distribution. Si NDs exhibit ultra-high density (1.4×10^{12} cm^{-2}), perfect uniformity (8.7 nm $\pm$ 10.1%), and quasi-crystal alignment. Similar to CB and VB formation, this perfect superlattice can also induce the periodic potential to form minibands.

(small exciton Bohr radius of 4.9 nm) in Si QDs have moved researchers' attention to III–V QDs grown by MBE. Coupled QD superlattices are also a valuable issue in quantum mechanics [22]. Very recently, a top-down nano-fabrication technology, damage-free neutral beam etching (NBE) combined with the self-assembled ferritin bio-template, is utilized to fabricate a high-quality Si nanodisk (ND) superlattice. In this study, we are dedicated to investigating the quantum design with the feasible nanotechnology for the Si-based IBSC. For this purpose, we develop a 3D finite element method (FEM) to calculate the electronic structure of a realistic QD superlattice, qualitatively discuss its optical and electrical properties, and analyse its potential application for a solar cell. Finally, a detailed limitation efficiency plot is calculated for the optimal quantum design of an Si-based IBSC.

2. Top-down process and theoretical model

Compared to kinetic-driven bottom-up nanotechnologies, top-down nanotechnologies are more attractive for ideal fabrication and direct engineering of superlattices. However, the traditional top-down process, for example the lithography process, is hardly implanted into quantum size fabrication.

The first difficulty is that common plasma etching unavoidably damages semiconductors by forming many defects, which act as recombination centers to degrade optical and electrical properties. The second difficulty is that the semiconductor exciton Bohr radius (Si = 4.9 nm) is far smaller than the minimum limitation of the photolithographic mask. Our developed NBE system effectively eliminates charged particles and UV photons to achieve finitely controllable and damage-free etching [23–25]. Thanks to stable DNA replication, the ferritin molecules can make various kinds of uniform sub-10 nm nanoparticles and can easily self-assemble to form an in-plane crystal-like structure, which can be used as an ideal nano-mask [26]. In addition, the one-step top-down etching ensures an ideal vertical alignment in stacked layers.

A simple fabrication flow is shown in figure 1(a). (i) Poly-Si and silicon dioxide (SiO$_2$) or silicon carbide (SiC) layers were alternately sputtered on substrates. The *in situ* monitoring was used to precisely control thickness. (ii) Ferritin molecules self-assembled to form a 2D array with the spin-coating method. Then the sample was heated in oxygen atmosphere at 500 °C for 1 h to remove protein shells and obtain a 2D array of metal oxide cores, an ideal etching mask. (iii) The oxidation surface was isotropically etched by the NF$_3$ gas/hydrogen radical at

Table 1. List of material parameters adopted in our calculations.

	Si	SiC
Electron effective mass	$0.27m_0$[26]	$0.394m_0$[27]
Heavy hole effective mass	$0.59m_0$[26]	$1.2m_0$[27]
Conduction band-offset		0.5 eV[26]
SiC bandgap		2.3 eV[27]

$100\,°C$ (hereafter called the 'NF$_3$ treatment'), and then was anisotropically etched by Cl2 NB to form NDs. Finally, various kinds of matrix material were re-sputtered to finish high-periodical Si superlattices. Figure 1(b) shows scanning electron microscope (SEM) images (before re-sputtering), which prove an ultra-high-quality Si ND superlattice with high uniformity and crystal-like alignment. The up-right scaled figures clearly exhibit quasi-hexagonal symmetry, very similar to the prime unit of a wurtzite crystal. Analogous to CB and VB formation in crystals, this high-periodical alignment indicates a possible miniband formation. Our NDs also exhibit high uniformity with a size distribution less than 10.1% in a 0.5 nm interval. The sheet density of one layer is up to 1.4×10^{12} cm^{-2}, two or three orders higher than any other methods. For example, the total density of 100-layers of InAs QDs is only 4.2×10^{12} cm^{-2}, perhaps the highest record in mature MBE [27]. The low QD density in prototype IBSCs is one of main reason for nonideal conversion efficiency.

This top-down process brings a great flexibility in quantum design, such as independently controllable diameter and thickness, various matrix materials, alignment symmetric and so on. It also means a great challenge for the existing theoretical model. In this paper, a 3D model is developed to calculate the coupled wavefunction and electronic structure, qualitative analyse optical/electrical properties and finally guide IBSC design.

From the envelope function theory, we solve 3D Schrödinger equations [28]

$$-\nabla \cdot \left(\frac{h^2}{2m} \nabla \phi \right) + V\phi = E\phi, \quad (1)$$

where h, m, V, E, ϕ are Planck's constant divided by 2π, the effective mass, the position-dependent potential energy, quantum levels, and the electron envelope function, respectively. We adopted Dirichlet conditions on the outer boundary (ten times larger than the Si ND superlattice) and continuous boundary conditions on the interface between ND and the matrix. Table 1 lists the calculation parameters [29, 30]. The crystalline Si greatly depends on the deposition process. For a wider application, we adopted the isotropic effective mass approximation. Of course, FEM can easily use the anisotropic effective mass to describe the concrete case.

Due to the limitations of nanotechnology, very few researchers paid enough attention to the analysis of current transportation in in-plane coupled QDs. Kuo *et al* developed the Anderson model to tentatively predict this coupling effect [31]. Following his model, we qualitatively analyse the special current–voltage (*I–V*) properties in Si ND

superlattices,

$$J = \frac{2eN}{h} \int_0^\infty d\varepsilon_z \int dk_{xy} \{ f_t[\varepsilon(k) - Ef_t]$$

$$- f_d[\varepsilon(k) - Ef_d] \} \cdot \frac{\Gamma_t \Gamma_d}{\Gamma_t + \Gamma_d} \text{Im} G_\sigma^r[\varepsilon(k), E(k_{xy})], \quad (2)$$

where N is the in-plane number of quantum dots, f_t is the Fermi-distribution function in the top contact and bottom contact respectively, Γ_t is the maximum tunneling rate, $\varepsilon(k)$ is the injection carriers' energy, the retarded Green function G includes the attribution of wavefunction coupling. The tunneling rates are calculated as a function of energy and momentum. In this study, we want to qualitatively analyse the miniband effect on carrier transportation. Therefore, according to [31], we define the relative unit, $J_0 = (2eN/h)(2m \times Ef_0/\hbar^2)\Gamma_t\Gamma_d/(\Gamma_t + \Gamma_d)$, where $Ef_0 = 20$ meV. To exclude conductivity differences of bulk materials, the bias is defined as the potential drop under the Si NDs, $V_0 = \frac{C_{\text{dot}}}{C_t + C_{\text{dot}} + C_d} V$, where C is the resistance in the top/down tunneling junction and the quantum resistance. Due to quantum resistance, h/e^2 is only 25.81 kΩ, which is far smaller than the tunneling junction, around 1–5 GΩ [32]. The main feature in our experiments is the lowered voltage threshold in the Si/SiC superlattices [33]. Here, we have only given the *I–V* curves via ground-state tunneling for simplicity while sacrificing accuracy.

Finally, the efficiency of IBSCs is deduced by using the detailed balanced equation [15–18]

$$\nabla \cdot \mathbf{J} = q(G_{VC} - R_{CV} + G_{IC} - R_{CI}), \quad (3)$$

where $\mathbf{J}$ is the photocurrent, q is electron charge, G is the carrier generation rate, and R is recombination rate. The IB is placed in the intrinsic area and only the photo-filling process is considered. The 6000 K black body radiation is used to simulate the AM 0 sunlight. The carrier generation and recombination rate are described as the classic thermodynamic equilibrium [15, 16], and free carrier absorption and non-radiative recombination strongly depend on the material's growth processes and thus can be neglected in the present studies. The VB includes light hole, heavy hole, and split-off states. In particular, a light hole in Si has a small effective mass, even far smaller than an electron's, which means a wider miniband. Thus, VB-derived minibands easily overwrite each other to form quasi-continuous bands. In addition, intraband transition in the CB has been widely proved in many material systems. Thus, in this study, we consider using the CB-derived minibands as the candidate for achieving a two-photon transition.

The main development lies in combining the quantum mechanical effect with the classic two-photon-transition model. It is known that the FEM is a powerful tool to simulate the realistic superlattice. A widely used model is the classic Kronig–Penney method [34–36]. However, this model can only describe a simple square or cubic QD in a high-dimensional system with an independent potential approximation. In this study, we develop an FEM simulation program to describe the arbitrary shape and alignment of the QD superlattice. For comparison, we consider a simple square
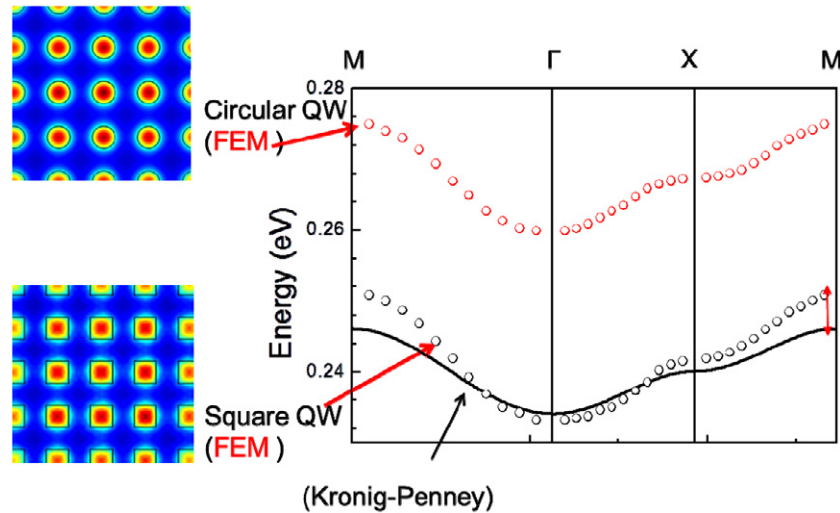
Figure 2. The $E - K$ dispersions in the square quantum wire superlattice calculated by the Kronig–Penney model (solid line) and FEM (black dot plots), and in the circular quantum wire superlattice calculated by the FEM (red dot plots). The Kronig–Penney method underestimates the $E - K$ dispersion, especially along the Γ–M direction, where the periodic potential in this model is overestimated. In addition, the Kronig–Penney method cannot deal with an arbitrarily shaped superlattice.

quantum wire superlattice with both the Kronig–Penney model and FEM. In the isolated QDs, the wavefunction is localized and forms a series of discrete levels; with increasing the QD numbers, their wavefunctions couple with each other and result in the level splitting, finally forming broad minibands in infinite superlattices. Here, the number of states in every miniband is equal to the number of QDs, and the Bloch vector has the following relationship to the sub-level space vector, $k = i\pi/(Nd + d)$, $i = 1, \ldots, N$. With it, FEM accurately calculates the minibands' structure for realistic quantum structures. Figure 2 exhibits the calculation results of a square quantum wire superlattice with two methods. The overall trends of the two methods are very similar. Due to effects of periodic potential, the ground level gradually increases along the Γ–X–M crystal direction, and returns to the Γ point, which forms a 2D in-plane miniband. The further comparison reveals that in this 2D case, the Kronig–Penney method underestimates the $E - K$ dispersion, especially along the Γ–M direction, the diagonal direction. The difference is near to 5 meV around the M point. From this it follows that the independent potential approximation in the high-dimensional Kronig–Penney model overestimates the potential in the diagonal zone to decrease the wavefunction diffusion probability into the neighboring dots [34]. In addition, FEM is particularly suitable for a realistic QD superlattice, which can easily consider components of arbitrary shape or symmetric and possibly inhomogeneous or a defect. For example, the circular quantum wire (red dot plot) superlattice with diameter equal to the square length has higher confinement energy, 40 meV in our structure. We want to emphasise that unlike common spherical QDs, the independently controllable diameter and thickness of NDs breaks the symmetry of the atomic orbit so that the three-fold degenerate p-orbit becomes a two-fold degenerate (121) state and non-degenerate (210) state. Here, we used three quantum numbers to define its state. This asymmetry

brings greater flexibility to miniband design for potential IBSC applications.

3. Results and discussion

3.1. Miniband formation and optical/electrical properties

Solar cell operation mainly includes the below processes, light absorption, recombination, and carrier collection. Ultraviolet and visible absorption spectroscopy and conductivity atomic force microscopy are used to evaluate the optical and electrical properties of the Si-NDs superlattice at room temperature.

The top-down process provides an extra degree of freedom on various matrices without considering growth kinetic limitations, such as interfacial chemical bonding, lattice or thermal matching, and so on. Several common matrices for Si QDs are Si_3N_4, SiC, and SiO_2. A distinct difference is the lower band-offset in Si/SiC than that in Si/SiO_2. Jiang *et al* predicted that this lower band-offset increases wavefunction expansion [35]. The Wannier functions calculated by the 3D FEM clearly reveal electron states exponentially decaying and penetrating from a superlattice site to nearest neighbors, as shown in figure 3(a). Due to the lower band-offset of Si/SiC, wavefunctions more easily diffuse into neighbors. This coupling relaxes the transition selection rule to induce additional optical transition beside the normal transition originating from the same superlattice site. High-intensity light illumination, a common operation condition of solar cells, excites these additional transitions to increase the total absorption. We fabricated two Si ND superlattices with 6.4 nm-diameter, 4 nm thickness, and 2.3 nm-interdot space embedded in a SiC matrix and a SiO_2 matrix, and measured their optical absorption coefficients with an ultraviolet–visible (UV–VIS) spectrometer. The results are shown in figure 3(b). Compared to the Si ND superlattice embedded in SiO_2, the same size
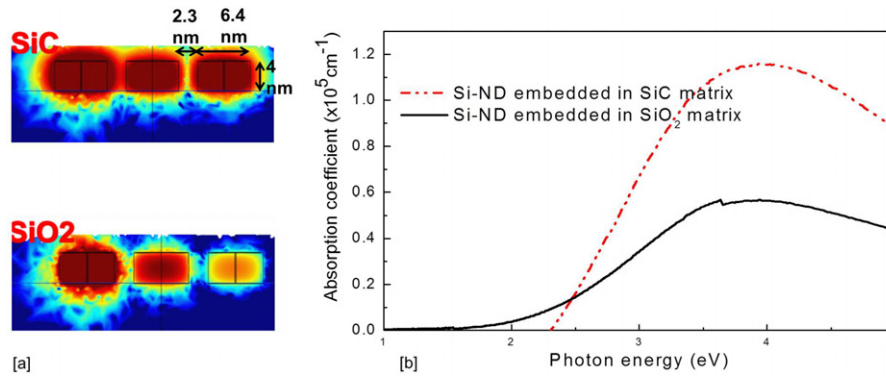
Figure 3. (a) Ground-state electron wavefunction distribution in the Si ND superlattice embedded in a SiC matrix and SiO₂ matrix. Due to the lower band-offset of SiC, wavefunctions more easily couple with neighbors, which relaxes the selection rules to induce additional optical transitions. (b) Optical absorption spectra of a 4 nm-thick, 6.4 nm-diameter, and 2.3 nm-interdot space Si ND superlattice. In changing the matrix from SiO₂ to SiC, the total absorption coefficient (2.0–5.0 eV) increases from 1.2 to 2.3×10^6 cm^{-1}, which indicates a greatly enhanced solar light capture.

superlattice embedded in the SiC matrix exhibits a remarkable enhancement of optical absorption coefficient even below the SiC bandgap. This result is consistent with the theoretical discussion and indicates an in-plane miniband formation in closely coupled Si ND superlattices.

The current density is calculated with the Anderson model, where ND coupling is described as the miniband width in the retarded Green function. Carrier transportation in the ND superlattice mainly depends on the resonant tunneling whose joint-state-density nearly follows a quasi-Gaussian distribution around the resonant peak, as shown in figure 4(a); coupled NDs form in-plane minibands to broaden resonant levels and thus increase the total tunneling probability, as shown in figure 4(b). Figure 4(c) exhibits the miniband structure in realistic Si ND superlattices. Due to the stronger wavefunction coupling, the ground miniband width increases from 0.37 meV in SiO₂ to 1.04 meV in the SiC matrix. The calculated $I–V$ property is shown in figure 4(d). Even excluding dielectric constant differences between the SiO₂ and SiC matrix, the stronger coupling remarkably enhanced conductivity. This theoretical prediction has been verified with conductivity atomic force measurements (c-AFM) on the same structure of Si ND embedded in a SiC matrix and SiO₂ matrix [33]. We note that the carrier transportation in minibands directly determined the photocurrent in the all-Si tandem solar cell. However, the intermediate band in IBSCs is isolated without the circuit, which does not directly contribute to photocurrent but affects the IB filling states to change the absorption/recombination process.

Experiments and calculations prove SiC as a promising matrix for solar cell applications and our Si ND superlattice has enough excellent optical/electrical properties to overcome degradations of open-circuit voltage and short-circuit current in common QD prototype cells [37].

3.2. Geometry-controlled electronic structure

The two-photon transition in IBSCs is determined by the intermediate band (IB) structure. The quantum confinement

effect provides the possibility to engineer nanomaterial electronic structure by controlling geometry size and material. According to the above discussions, SiC is chosen as the matrix. A detailed and systematic 3D-plot is shown in figure 5(a) to clarify electronic structures in various possible geometries. The sectional graphs, figures 5(b)–(d), exhibit the electronic structures' dependences on thickness, diameter, and interdot space, respectively. Several important features are explained as follows: (i) miniband positions decrease inverse-squarely with increasing thickness and diameter, which originates from the classic quantum confinement; (ii) the interdot space only dominates the wavefunction expansion to change the minibands width but not affect the miniband position; (iii) due to wavefunction in-plane coupling, the minibands' width strongly depends on the diameter and is basically independent of the thickness. Our previous experiment has revealed an asymmetric enhancement optical absorption with independently shrinking ND diameter and thickness, which indirectly proves the asymmetric in-plane miniband dependence [25].

3.3. IBSC design

Suggested device structure and device energy band are shown in figures 6(a) and (b). The Si/SiC ND superlattice acts as the absorption layer via two-photon-transition where IB positions combine two low-energy photons to generate extra photocurrent. The large bandgap matrix supports a large photovoltage, $V = u_{cv}/e$, where u_{cv} is the chemical potential difference between CB and VB, but increases the optical penetration. Our calculation reveals that 3C-SiC has a proper bandgap to efficiently match the solar cell spectrum. In addition, thanks to the miniband formation, the Si ND superlattice embedded in SiC is proved to have a high optical absorption and electrical conductivity, which have the potential to be further improved by optimizing deposition, etching, and annealing processes. In this study, we tried to deduce some universal quantum designs with feasible nanotechnology. Thus, we deduced the limitation efficiency
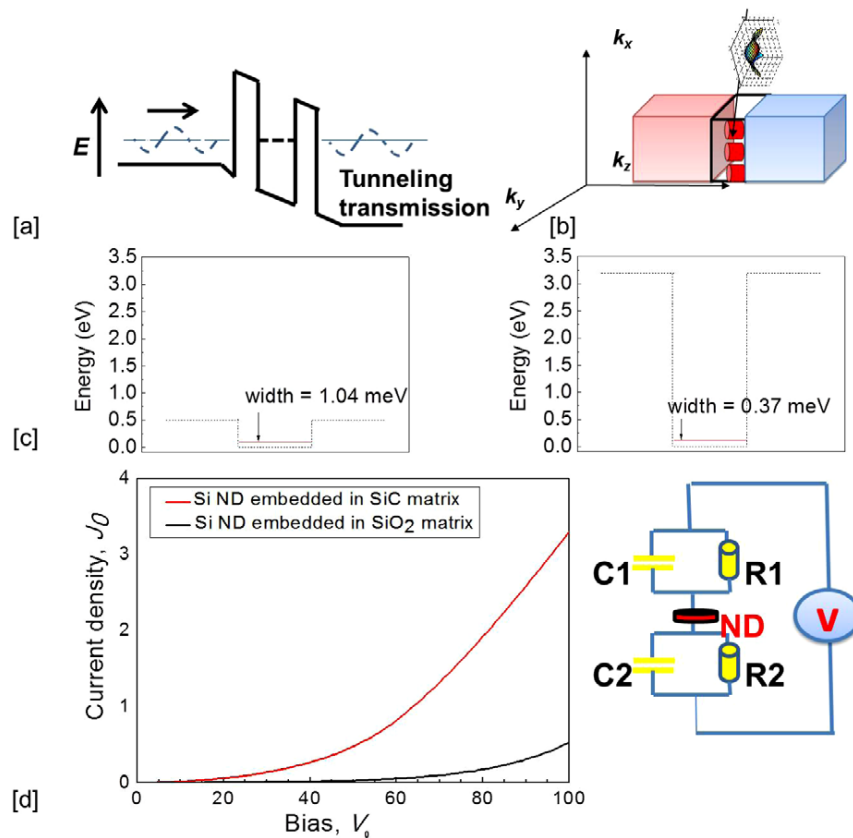
Figure 4. Electrical conductivity of the 4 nm-thick, 6.4 nm-diameter, and 2.3 nm-interdot space Si ND superlattice. (a) Resonant tunneling dominates carrier transport. (b) The in-plane miniband broadens the resonant level to increase the joint-state-density of the resonant tunneling. (c) In changing the matrix from SiO_2 to SiC, the in-plane miniband broadens from 0.37 to 1.04 meV. (d) The calculated *I–V* plot exhibits a better conductivity due to the wider miniband formed with the SiC matrix.

in ideal materials with infinite thickness and without any electrical resistant loss. The p–n junction of 3C-SiC induces an internal built-in potential field to separate and transport electrons/holes to the external circuit. A great advantage in IBSCs is concise and feasible device structure, especially compared to Si tandem solar cells including abundant multi-heteroepitaxy and tunneling junctions.

The first precondition of IB is miniband formation in the ND superlattice with highly periodical alignment and strong enough wavefunction coupling. Past studies reveal that non-uniform size and alignment result in wavefunction localizations in lattice defects to form isolated quantum levels rather than continuous minibands [38], which is also confirmed in our simulations. The stable DNA replication in our bio-template resolves this problem well; for the first time, a quasi-crystal-like Si QDs superlattice has been fabricated on various substrates (figure 1(b)). Due to large effective masses in Si, the interdot space limitation is suggested by calculations to be less than 3 nm, as shown in figure 5(d). Our 2D array satisfied these strict requirements with only 2.2 nm separation. The second key limitation is that the miniband should be separated from the continuous CB and VB with sub-gaps larger than the thermal energy. Independently adjusting diameter and thickness can broaden specific minibands and cause miniband degeneration or non-degeneration to form one-level or multi-level IB separated from the CB and VB. This process is determined by both the quantum size effect

and wavefunction coupling so that none of the monotonous relationship can be extracted. A feasible method is to calculate electronic structures in various possible structures, figure 5, to seek proper IBs.

Referring to figure 5, a periodical Si-NDs array can be carefully designed to operate as a one-level or multi-level IBSCs. The two-photon transition is described as the detailed balanced equation. The efficiency contour plots were calculated to guide IBSC design, as shown in figure 7. Notably, the maximum efficiency is 50.3% under the full concentration, which is very promising, compared with Si solar cells. Only by not considering the current degradation in the tunneling junction, does the two-junction Si tandem solar cell have a comparative efficiency. In our studies, the optimal structure is a 5 nm-diameter, 5 nm thickness, and 2 nm inter-space, hexagonal Si ND superlattice. Due to miniband degeneracy in various structures, the conversion efficiency exhibits multiple second peaks and depends sensitively on superlattice structures. Referring to figure 7, other structures can also be considered to balance process difficulties and theoretical efficiency.

4. Conclusions

For the first time, we made a realistic quantum design of Si-based IBSCs according to the feasible Si nanotechnology. By combining self-assembled bio-template and damage-free
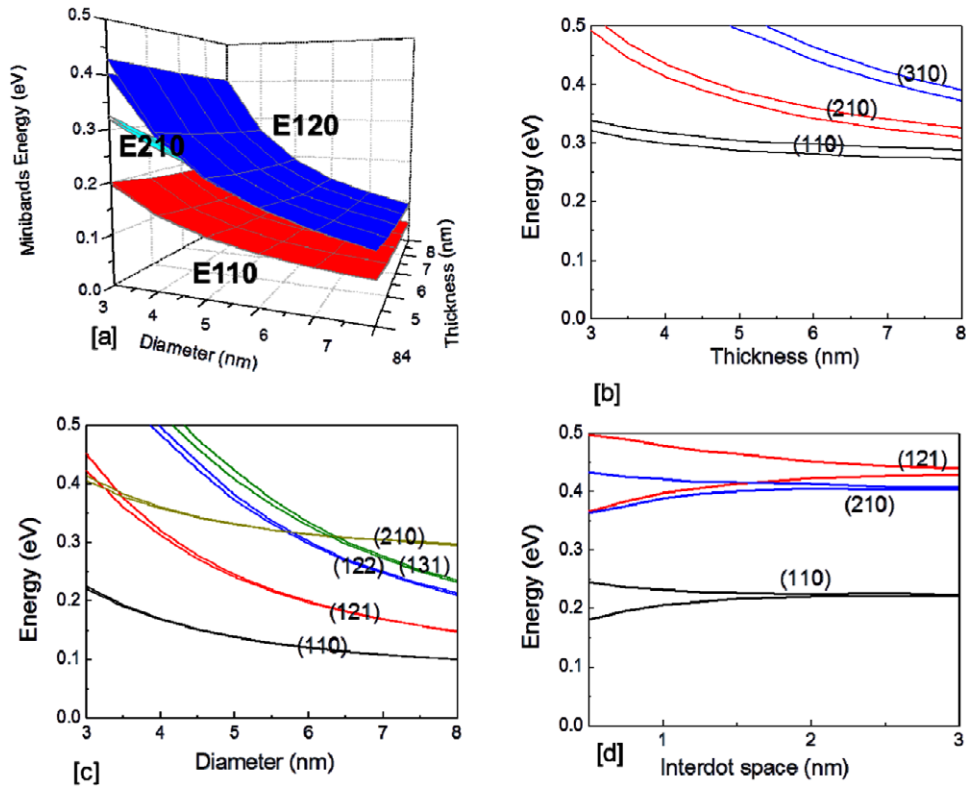
Figure 5. (a) Systematic miniband engineering in Si NDs embedded in the SiC matrix. Minibands' dependence on (b) Si ND thickness (diameter = 2 nm, interdot space = 2 nm); (c) diameter (thickness = 3 nm, interdot space = 2 nm); (d) interdot space (diameter = 3 nm, thickness = 3 nm). Due to the quantum size effect, increasing the thickness or diameter inverse-squarely lowers the minibands; however, due to asymmetric crystal structure, only increasing diameter remarkably decreases miniband widths. The interdot space only affects miniband widths.
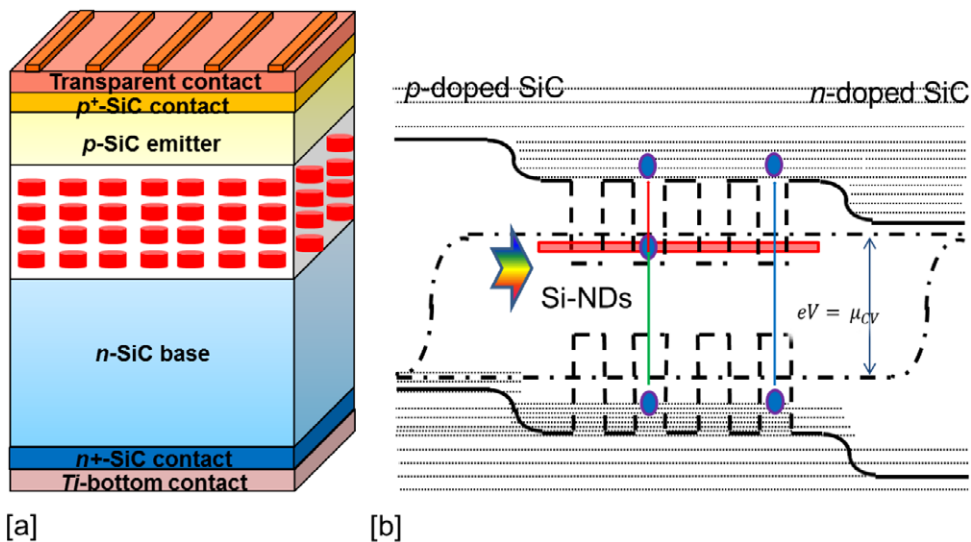

Figure 6. (a) A suggested device structure consists of a Si ND superlattice inserted into a SiC p–n junction. This concise and feasible structure avoids complex multi-heteroepitaxy and a difficult tunneling junction in tandem cells. (b) The device energy band diagram. Two-photon transition is achieved via optimized electron minibands (IBs), which extend solar spectrum coverage without losing the photovoltage.

NBE, an advanced top-down process is developed to fabricate sub-10 nm, high uniformity and density, and highly periodical QD superlattices. A 3D FEM has been advanced to calculate minibands with arbitrary shape and arrangement of the Si QD superlattice. Our calculation qualitatively proved that in-plane coupling enhanced optical absorption coefficients and electrical conductivity. A conversion efficiency of 50.3% is predicted for the novel Si-based IBSC. Detailed electronic structure and conversion efficiency are examined to guide optimal design of IBSCs. Our designed structure breaks
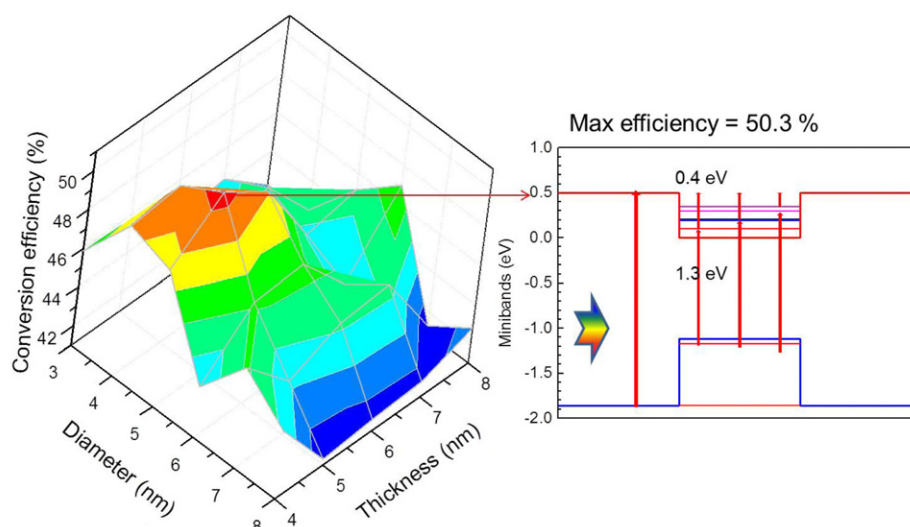
Figure 7. The efficiency contour plot depends on the Si ND quantum structures. The maximum efficiency is 50.3% under the full concentration, which is comparable to a complex Si tandem solar cell.

through the S–Q limit in Si solar cells, and has the potential to be integrated into current Si photovoltaic processes.

References

[1] Green M A, Emery K, Hishikawa Y, Warta W and Dunlop E D 2012 *Prog. Photovolt., Res. Appl.* **20** 606–14
[2] Luque A, Martí A and Stanley C 2012 *Nature Photon.* **6** 146–52
[3] Luque A and Martí A 1997 *Phys. Rev. Lett.* **78** 5014–7
[4] Sablon K A, Little J W, Mitin V, Sergeev A, Vagidov N and Reinhardt K 2011 *Nano Lett.* **11** 2311–7
[5] Palacios P, Aguilera I, Sanchez K, Conesa J C and Wahnon P 2008 *Phys. Rev. Lett.* **101** 046403
[6] Okada Y, Morioka T, Yoshida K, Oshima R, Shoji Y, Inoue T and Kita T 2011 *J. Appl. Phys.* **109** 024301
[7] Ahsan N, Miyashita N, Islam M M, Yu K M, Walukiewicz W and Okada Y 2012 *Appl. Phys. Lett.* **100** 172111
[8] Song T, Zhang F, Lei X, Xu Y, Lee S and Sun B 2012 *Nanoscale* **4** 1336–43
[9] Zhang G, Finefrock S, Liang D, Yadav G G, Yang H, Fang H and Wu Y 2011 *Nanoscale* **3** 2430–43
[10] Bakke J R, Pickrahn K L, Brennan T P and Bent S F 2011 *Nanoscale* **3** 3482–508
[11] Yang Z, Shi Y, Liu J, Yan B, Zhang R, Zheng Y and Wang K 2004 *Mater. Lett.* **58** 3765–8
[12] Antolín E, Martí A, Farmer C D, Linares P G, Hernández E, Sánchez A M, Ben T, Molina S I, Stanley C R and Luque A 2010 *J. Appl. Phys.* **108** 064513
[13] Lin A and Phillips J 2009 *IEEE Trans. Electron Devices* **56** 3168–74
[14] Yoshida K, Okada Y and Sano N 2010 *Appl. Phys. Lett.* **97** 133503
[15] Luque A, Linares P G, Antolín E, Cánovas E, Farmer C D, Stanley C R and Martí A 2010 *Appl. Phys. Lett.* **96** 013501

[16] Nozawa T and Arakawa Y 2011 *Appl. Phys. Lett.* **98** 171108
[17] Hu W G, Inoue T, Kojima O and Kita T 2010 *Appl. Phys. Lett.* **97** 193106
[18] Tomić S, Jones T S and Harrison N M 2008 *Appl. Phys. Lett.* **93** 263105
[19] Tomić S 2010 *Phys. Rev.* B **82** 195321
[20] Aeberhard U 2012 *Opt. Quantum Electron.* **44** 133
[21] Hu W, Harada Y, Hasegawa A, Inoue T, Kojima O and Kita T 2011 *Prog. Photovolt. Res. Appl.* doi:10.1002/pip.1208 (early view)
[22] Harman T C, Taylor P J, Walsh M P and LaForge B E 2002 *Science* **297** 2229–32
[23] Samukawa S, Kubota T, Huang C-H, Hashimoto T, Igarashi M, Nishioka K, Takeguchi M, Uraoka Y, Fuyuki T and Yamashita I 2008 *Appl. Phys. Express* **1** 074002
[24] Igarashi M, Huang C-H, Morie T and Samukawa S 2010 *Appl. Phys. Express* **3** 085202
[25] Budiman M F, Hu W, Igarashi M, Tsukamoto R, Isoda T, Itoh K M, Yamashita I, Murayama A, Okada Y and Samukawa S 2012 *Nanotechnology* **23** 0653021
[26] Tsukamoto R, Igarashi M, Samukawa S and Yamashita I 2012 *Appl. Phys. Express* **5** 065201
[27] Oshima R, Okada Y, Takata A, Yagi S, Akahane K, Tamaki R and Miyano K 2011 *Phys. Status Solidi* c **8** 619–21
[28] Voss H 2006 *Comput. Phys. Commun.* **174** 441–6
[29] Conibeer G *et al* 2008 *Thin Solid Films* **516** 6748–56
[30] Wu W L, Fan J Y, Qiu T, Yang X, Siu G G and Chu P K 2005 *Phys. Rev. Lett.* **94** 026102
[31] Kuo D M-T, Guo G Y and Chang Y C 2001 *Appl. Phys. Lett.* **79** 3851–3
[32] Zaknoon B and Bahir G 2008 *Nano Lett.* **8** 1689–94
[33] Igarashi M, Budiman M F, Pan W, Hu W, Tamura Y, Syazwan M E, Usami N and Samukawa S 2013 *Nanotechnology* **24** 015301
[34] Lazarenkova O L and Balandin A A 2001 *J. Appl. Phys.* **89** 5509–15
[35] Jiang C-W and Green M A 2006 *J. Appl. Phys.* **99** 114902
[36] Rodríguez-Bolívar S, Gómez-Campos F M, Luque-Rodríguez A, López-Villanueva J A, Jiménez-Tejada J A and Carceller J E 2011 *J. Appl. Phys.* **109** 074303
[37] Igarashi M, Budiman M F, Pan W, Hu W, Tamura Y, Syazwan M E, Usami N and Samukawa S 2012 *Appl. Phys. Lett.* **101** 063121
[38] Littleton R K and Camley R E 1986 *J. Appl. Phys.* **59** 2817–20